Ignition of hydrogen-air mixtures by a localized stationary hot surface

R. Mével [a], J. Melguizo-Gavilanes [a], L.R. Boeck [a], A. Nové-Josserand [b], Y. Kishita [c], S. Coronel [a] & J.E. Shepherd [a]

E-mail: *mevel@caltech.edu*

[a] California Institute of Technology, Pasadena, USA
[b] Ecole Polytechnique Paris, Paris-Saclay, France
[c] Tokyo Institute of Technology, Tokyo, Japan

Abstract

In the present study, the ignition of hydrogen-air mixtures by a stationary hot glow plug has been investigated. The ignition process was characterized by the surface temperature when ignition occurs, as well as by the location where the initial flame kernel is formed. The experimental results indicate that the ignition temperature threshold is a function of equivalence ratio whereas the ignition location is a function of the rate at which the glow plug is heated. Comparison with two-dimensional numerical simulations exhibits significant discrepancies in terms of the temperature threshold evolution with equivalence ratio. These results indicate that a number of parameters, including surface temperature non-uniformity, surface chemistry and reaction model used, could influence the ignition threshold as well as the location of ignition.
Keywords: *Hot surface ignition, industrial safety, hydrogen, numerical simulation*

1. Introduction

The accidental ignition of reactive mixtures and subsequent flame propagation is a major safety concern for a number of industrial activities such as commercial aviation, chemical processes, nuclear energy production, and mining. Heated surfaces represent a potential hazard that needs to be assessed in order to prevent and mitigate accidental combustion events. For hot surface ignition, several cases can be differentiated based on two important parameters. The first one is whether the surface is stationary or moving. The second one is the size, i.e. area, of the hot surface. In the case of stationary hot surfaces, two ignition regimes exist, low and high temperature ignition. In the case of extended large surfaces, low-temperature (T<800K) ignition needs to be considered. This latter configuration is more relevant to hydrocarbon fuels like *n*-alkanes which exhibit auto-ignition temperature on the order of 500 K as reported by Colwell and Reza (2005), Kuchta et al. (1965) and Council (1983). In the case of localized small surfaces, high-temperature (T>800K) ignition has to be considered. The present study focuses on a stationary localized surface with an imposed heating rate. This configuration was studied Roth et al. (2014), Beyer

and Markus (2012), Dubaniewicz (2006), Dubaniewicz et al. (2003), Dubaniewicz et al. (2000), Bothe et al. (1999), Homan (1981), Boettcher et al. (2013), Boettcher (2012), and Menon et al. (2016). These previous studies demonstrated the importance of a number of parameters such as the mixture chemical properties and surface properties (geometry, material) on the surface temperature required for ignition to take place. To our knowledge, few of the previous studies investigated the effect of the hot surface heating rate on the ignition threshold and ignition location (relative to the hot surface). In the low-temperature regime, Boettcher et al. (2012) and Melguizo-Gavilanes et al. (2015) showed that the heating rate of an extended hot surface is the dominant parameter which determines the type of reaction, i.e. slow oxidation versus rapid explosion, that the reactive mixture undergoes. For a small hot surface, Menon et al. (2016) have shown that for *n*-hexane-air mixtures, the chemical processes characteristic of the negative temperature coefficient region influence the ignition phenomenon. Consequently, the heating rate, which determines the time spent by the mixture at a temperature close to the ignition temperature, could influence the ignition behavior by a localized hot surface.
The goal of the present study was to characterize the ignition of hydrogen-air mixtures in terms of ignition threshold and ignition location for different heating rates using a specific hot surface (a diesel engine glow plug) that has been used in some previous studies in our laboratory. Corresponding numerical simulations were performed to obtain insights into the dynamics of the ignition process.

2. Experimental set-up

2.1 Combustion vessel

The ignition experiments were performed in a closed vessel with a volume of approximately 2 L. The vessel inner dimensions were 114 mm x 114 mm x 171 mm. Quartz windows on each side of the vessel allowed for optical access. An electrically heated glow plug (Autolite 1110 Glow Plug) was used as the hot surface. The hot surface was a vertical cylinder approximately 9.3 mm in height and 5.1 mm in diameter. The glow plug was connected to a low voltage (5-15 V) power supply for heating and placed at the center of the bottom plate of the vessel. The power supply current was varied to obtain different heating rates. Quasi-constant heating rates were achieved by maintaining constant current. A pressure transducer (Heise model 901A) located on the filling line of the vessel was used to prepare the mixtures using the partial pressure method.

2.2 Surface temperature measurement

A two-color pyrometer was used to make non-contact measurements of the glow plug surface temperature by comparing the radiation emitted by the hot glow plug at two different near-infrared wavelengths, 1705 and 1940 nm, emitted by the hot glow plug. The relationship between intensities of each wavelength λ and temperature T is derived from Plank's law for a hot body. Plank's law is approximated if λ is small ($\lambda T \ll C_2$). Therefore, the irradiance $L_\lambda(T)$ is written as $L_\lambda(T) \approx \varepsilon_\lambda \frac{C_1}{\lambda^5} \exp\left(\frac{-C_2}{\lambda T}\right)$, where ε_λ is the spectral emissivity, and C_1 and C_2 are Plank's radiation constants. The radiation intensity $I(T)$ is approximated if the region of integration $\Delta\lambda$ is small enough; $I(T) \approx \varepsilon_\lambda \frac{C_1}{\lambda^5} \exp\left(\frac{-C_2}{\lambda T}\right) \Delta\lambda$. The

relationship between the ratio of radiation intensities, I_1/I_2, at two wavelengths, λ_1 and λ_2, and temperature, T, is expressed as

$$\ln\left(\frac{I_1}{I_2}\right) = \frac{A}{T} + B \tag{1}$$

where $A = C_2\left(\frac{1}{\lambda_2} - \frac{1}{\lambda_1}\right)$ and $B = \ln\left(\frac{\lambda_2^5}{\lambda_1^5}\frac{\Delta\lambda_1}{\Delta\lambda_2}\right)$.
Equation 1 assumes wavelength-independent emissivity. However, for the glow plug material, stainless steel 316, a difference in emissivity of up to 2.5%, was reported by Touloukian and DeWitt (1970) between the two pyrometer wavelengths used. This translates into a measurement uncertainty (Coates (1981))

$$T = \left[\frac{1}{C_2}\cdot\frac{\lambda_1\lambda_2}{\lambda_2-\lambda_1}\cdot ln\left(\frac{\epsilon_1}{\epsilon_2}\right) + \frac{1}{T_m}\right]^{-1}, \tag{2}$$

where T is the real surface temperature, T_m is the measured temperature assuming wavelength-independent emissivity and ϵ_1 and ϵ_2 are the emissivities at the wavelengths λ_1 and λ_2, respectively. For example, evaluating Equation 2 at a real surface temperature of 1000 K yields a temperature uncertainty of $\pm$25 K. Further sources of uncertainty in the temperature measurement include: calibration uncertainty due to accuracy and stability of the calibration source; effect of signal noise; temperature difference between the location of temperature measurement (on the side of the glow plug, about 1 mm below the top) and the ignition location.

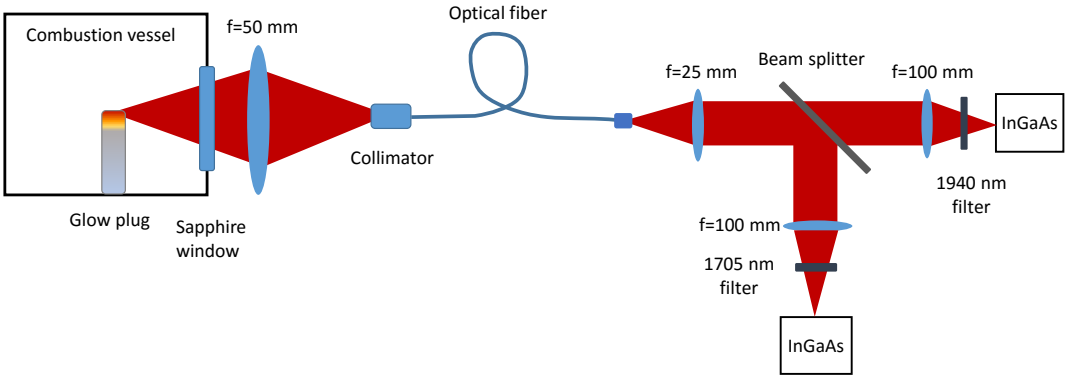

Figure 1: Schematic of the optical setup of the pyrometer.

Figure 1 shows a schematic of the two-color pyrometer used to measure the glow plug temperature. The light from the glow plug passed through a sapphire window, convex lens, collimator and optical fiber. Then, the beam was separated by a dichroic beam splitter with a cutoff wavelength of 1800 nm. After the beam splitter, each beam passed through bandpass interference filters: 1940 nm for the transmitted one, 1705 nm for the reflected one. Finally, the beams reach two InGaAs photo detectors that delivered an output voltage proportional to light intensity.

Two different calibration methods were used to obtain the coefficients A and B in Equation 1. The first method used the temperature measured by a K-type thermocouple in contact with the top of the glow plug as the reference temperature. The second method used a black body calibration source, BBS1200 model from Process Sensors. Figure 2 shows calibration curves of the pyrometer obtained with the thermocouple and the black body. The black body calibration was performed at three different black body aperture diameters for each temperature. As shown in Figure 2, aperture size does not have a significant effect on the calibration.

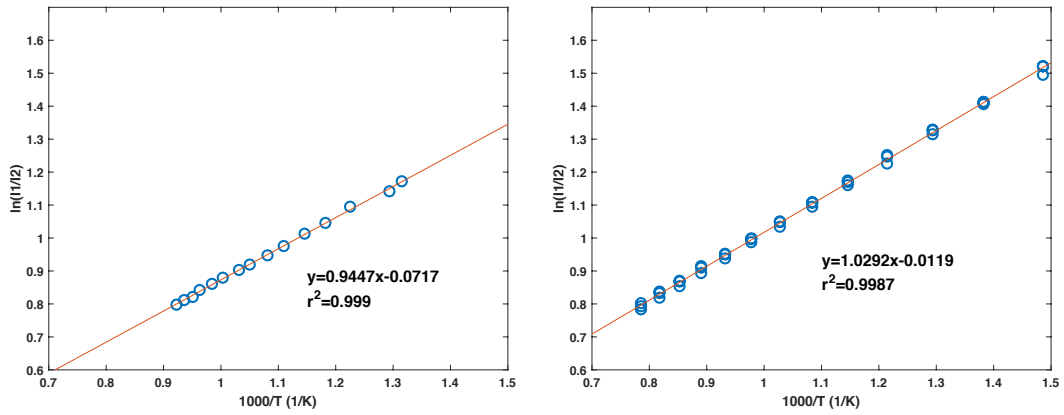

a) Thermocouple calibration b) Black body calibration

Figure 2: Calibration curves obtained for the two color pyrometer using a) a thermocouple and b) a black body calibration source.

2.3 Flow visualization

Figure 3 shows a schematic of the Mach-Zehnder interferometer used to visualize the gas density field in the vessel. A 532 nm solid state laser (Spectra Physics Excelsior) was used as the light source. The beam was expanded through a 18x beam expander and two convex lenses. The beam was then divided by a prismatic beam splitter cube, one beam was directed through the vessel and then turned with a mirror. The other beam was turned with a mirror and the two beams were then recombined through a second prismatic beam splitter cube. A 500 mm focal length converging lens between the cubic prism and high-speed camera (Phantom V 7-11) was used to locate the camera focus at the top of the glow plug location. The interferograms obtained with the Mach-Zehnder interferometer represent the optical path length difference between light traveling through a field of view with refractivity $n(z)$ and light traveling through a reference field with refractivity $n_0(z)$. In the current experiment configuration, z corresponds to the axis that is normal to the vessel windows. The optical phase difference, $\Delta\varphi$, is related to the index of refraction n by,

$$\Delta\varphi = \varphi - \varphi_0 = \frac{2\pi}{\lambda}\int_{\xi_1}^{\xi_2}[n(z) - n_0(z)]\,\mathrm{d}z, \tag{3}$$

where ξ_1 and ξ_2 are the locations along the $z-$axis where a ray of light enters and leaves the test section, respectively, and λ is the wavelength of the light source in a vacuum. In

the current study, $\lambda = 5.32 \times 10^{-7}$ m. The intensity, I, of a two-dimensional fringe pattern is represented by an amplitude and frequency modulated function,

$$I(x,y) = a(x,y) + b(x,y)\cos(\Delta\varphi(x,y)) \tag{4}$$

where a represents the background illumination and noise, b is the amplitude, and φ is the phase (Rastogi and Hack, 2015). The phase demodulation of the interferograms, i.e. obtaining $\Delta\varphi$, is accomplished by using the 2D Windowed Fourier Filtering method (WFF2) (Kemao, 2004).

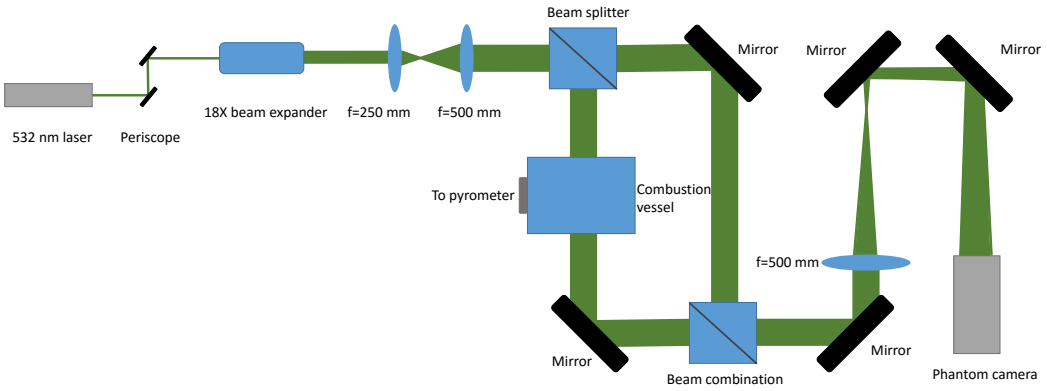

Figure 3: Schematic of the Mach-Zhender interferometer.

2.4 Experimental procedure

Before each experiment, the vessel was evacuated to below 10 Pa and filled with hydrogen, oxygen and nitrogen to create the desired mixture. The gases were then mixed using a circulation pump, and left to settle. The power supply was turned on to start heating of the glow plug. The gas temperature and pressure and the pyrometer signals were recorded using two digital recorders (Pico Technology PicoScope and LeCroy Wavesurfer 44 MXs). Two sets of experiments were performed, the first with a glow plug heating rate of 220 K/s, and the second with heating rates lower than 220 K/s.

3. Computational methodology

3.1 Governing equations

The motion, transport and chemical reaction in the gas surrounding the glow plug are modeled using the low Mach number, variable-density reactive Navier-Stokes equations with temperature-dependent transport properties.

$$\partial_t(\rho) + \nabla \cdot (\rho \mathbf{u}) = 0 \tag{5}$$

$$\partial_t(\rho \mathbf{u}) + \nabla \cdot (\rho \mathbf{u}\mathbf{u}) = -\nabla P + \nabla \cdot \tau + \rho \mathbf{g} \tag{6}$$

$$\partial_t(\rho Y_i) + \nabla \cdot (\rho \mathbf{u} Y_i) = -\nabla \cdot \mathbf{j_i} + \dot{\omega}_i \tag{7}$$

$$\partial_t(\rho h_s) + \nabla \cdot (\rho \mathbf{u} h_s) = -\nabla \cdot \mathbf{j_q} + \dot{q}_{\text{chem}} \tag{8}$$

$$P = \rho \bar{R} T, \quad \tau = \mu[\nabla \mathbf{u} + (\nabla \mathbf{u})^T] - \frac{2}{3}\mu(\nabla \cdot \mathbf{u})\mathbf{I} \tag{9}$$

In equations (3)-(7), ρ, P and T are the gas density, pressure and temperature, $\mathbf{u}$ is the velocity vector, h_s is the mixture sensible enthalpy, $\mathbf{g}$ is the gravitational acceleration, Y_i is the mass fraction of species, $\mathbf{j_i}$ is the species diffusion flux, $\dot{\omega}_i$ represents the rate of production/consumption of species, $\mathbf{j_q}$ is the heat flux, $\dot{q}_{\text{chem}} = -\sum_{i=1}^{N} \Delta h^o_{f,i} \dot{\omega}_i$ is the rate of conversion of chemical into thermal energy, $\Delta h^o_{f,i}$ is the enthalpy of formation of species, $\bar{R}$ is the specific gas constant, and μ is the mixture viscosity. The species diffusion term, $\mathbf{j_i}$, uses Fick's law for binary mixtures. For multicomponent mixtures where one component is present in large amounts (i.e. N_2 for combustion in air) all other species may be treated as trace species. Writing the binary diffusion coefficient with respect to N_2 only yields:

$$\mathbf{j_i} = -\rho D_i \nabla Y_i, \quad \text{with} \quad D_i = D_{j,N_2} \tag{10}$$

where D_i is the effective diffusion coefficient. In Equation 10, thermodiffusion or Soret effect was neglected. The approach proposed by Poinsot and Veynante (2005) was used to ensure mass conservation while using Fick's law.

The heat flux $\mathbf{j_q}$ includes the effect of partial enthalpy transport by diffusion

$$\mathbf{j_q} = -\frac{\kappa}{c_p}\nabla h_s + \sum_{i=1}^{N-1} h_{s,i}\left(\mathbf{j_i} + \frac{\kappa}{c_p}\nabla Y_i\right) \tag{11}$$

where κ and c_p are the mixture averaged thermal conductivity and specific heat, respectively. In Equation 11, the Dufour effect (i.e. energy flux due to a concentration gradient) was neglected as suggested by Smooke (2013). Substituting Equation 10 into Equation 11 yields:

$$\mathbf{j_q} = -\frac{\kappa}{c_p}\nabla h_s + \sum_{i=1}^{N-1} h_{s,i}\left(1 - \frac{1}{\text{Le}_i}\right)\frac{\kappa}{c_p}\nabla Y_i \tag{12}$$

where $\text{Le}_i = \kappa/(c_p \rho D_i)$ is the Lewis number of species i. The second term on the right hand side of Eq. 12 vanishes if the Lewis numbers of all species are assumed to be unity. This approximation is common in combustion codes but is not justified in many applications (Poinsot and Veynante (2005)).

The equations above were solved in an axisymmetric two dimensional geometry using the Open source Field Operation And Manipulation (OpenFOAM) toolbox (Weller et al. (1998)). The spatial discretization of the solution domain was performed using finite volumes. Specifically, the convective terms were discretized using a second order, bounded TVD scheme; the mass fractions were discretized using a linear centered scheme for scalars bounded between zero and one. The diffusion terms were discretized using the linear centered scheme together with a second order conservative scheme for the evaluation of the surface normal gradients. The linear systems that resulted from the discretization of the governing equations were solved through iterative techniques (Saad (2003)). The PBiCG (Preconditioned Biconjugate Gradient) method was used for all linear systems including the chemical source terms preconditioned through the DILU (Diagonal Incomplete-LU) technique, whereas the Poisson equation for pressure was solved using the PCG (Preconditioned Conjugate Gradient) preconditioned by the DIC (Diagonal Incomplete Cholesky). The pressure-velocity coupling was achieved using the PIMPLE

(PISO+SIMPLE) algorithm (Demirdzic et al. (1993)). Finally, the time-step was dynamically adapted during the course of the computation based on a specified Courant number to ensure stability of the numerical scheme (Oran and Boris (2001)). In the present study, the Courant number used is 0.2.

3.2 Chemical and transport models

The chemistry was modeled using Mével's (Mével et al., 2011), and Hong's (Hong et al., 2011) detailed mechanisms for hydrogen oxidation which includes 9 species and 21 reactions, and 10 species and 40 reactions, respectively. The Sutherland Law, modified Eucken relation and JANAF polynomials were used to account for the functional temperature dependence of mixture viscosity, thermal conductivity and specific heat, respectively. Species diffusivities were computed using Cantera (Goodwin et al. (2015)); a constant non-unity Lewis number, Le_i, was specified for each species. This is a convenient approximation since Le_i values are essentially constant and usually vary in small amounts across flame fronts (Poinsot and Veynante (2005)).

3.3 Domain, initial and boundary conditions

The geometry simulated approximately corresponded to that described in section 2., a cylindrical vessel of 11.4 cm x 17.1 cm with a glow plug of 9.3 mm x 5.1 mm located in the center. There were approximately 200,000 cells in the 2D-axisymmetric computational domain, compressed near the wall of the glow plug, with a minimum cell size of $80\,\mu$m to resolve the thermal and hydrodynamic boundary layers.
The initial conditions were $P_o = 101\,$kPa, $T_o = 300\,$K, $U_o = 0\,$m/s, and mass fractions $Y_{\mathrm{H_2}}, Y_{\mathrm{O_2}}, Y_{\mathrm{N_2}}$, corresponding to an equivalence ratio (hydrogen concentration by volume), Φ ($\%\mathrm{H}_{2,vol}$), ranging from 0.265 (10%) to 5.55 (70%). No-slip boundary condition and constant temperature $T_{wall} = T_o$ were imposed on the vessel walls, and on the glow plug surface, a prescribed temperature ramp was given by $T(t) = T_o + rt$ with $r = 220\,$K/s. This heating rate was the same as that used for the initial set of experiments, and higher than the one used for the second set of experiments. In order to quantify the effect of the heating rate on the ignition threshold simulations at 110 K/s and 440 K/s were performed. For the range of heating rate investigated, a difference in the prediction of the ignition threshold of 0.3 % was found, and deemed negligible in the present study. Note that simulations were not performed for the lower heating rates that were used in some later experiments due to limitations on computational run times.

4. Results and discussion

4.1 Experimental results

In order to characterize the ignition of hydrogen-air mixtures by a hot glow plug, the temperature of the glow plug when ignition occurred was measured using the two-color pyrometer. In addition, the location of the ignition was observed in the interferograms. Three different ignition locations were observed: (i) symmetric ignition above the top of the glow plug, (ii) asymmetric (off-center) ignition above the top of the glow plug, and

(iii) ignition to the side of the glow plug. Figure 4 shows an example of the experimental optical phase difference fields for each cases. Phase differences are reported rather than temperature which can only be obtained in the case of axisymmetric events. Figure 5 shows the evolution of the ignition threshold and ignition location as a function of equivalence ratio. In the initial series of experiments (Figure 5 a)), the maximum possible heating rate, 220 K/s, that could be obtained with our power supply was employed. For this series of experiments, the thermocouple calibration approach was employed. Under these conditions, the ignition temperature threshold was found to be around 950 K for equivalence ratios between 0.5 and 3. For richer mixtures, the temperature threshold shifted to about 1080 K. Concerning the ignition location, the initial flame kernel was observed to form preferentially on the side of the glow plug. In the later series of experiments (Figure 5 b)), the black body calibration was used, and lower heating rates, in the range 0.2-181 K/s, were employed. Under these conditions, the temperature threshold for ignition to occur increased linearly with equivalence ratios in the range 0.3 to 1.3 with T_{ign} ≈1050 K at Φ=0.3 and T_{ign} ≈1200 K at Φ=1.3. At higher equivalence ratios, Φ >2, the ignition threshold was about 1200 K, independent of both equivalence ratio and heating rate. For the slowest heating rate, ignition was observed to occur symmetrically above the top of the glow plug in most cases. Note that ignition thresholds of all three ignition locations coincided well for the slowest heating rate of 18 K/s.

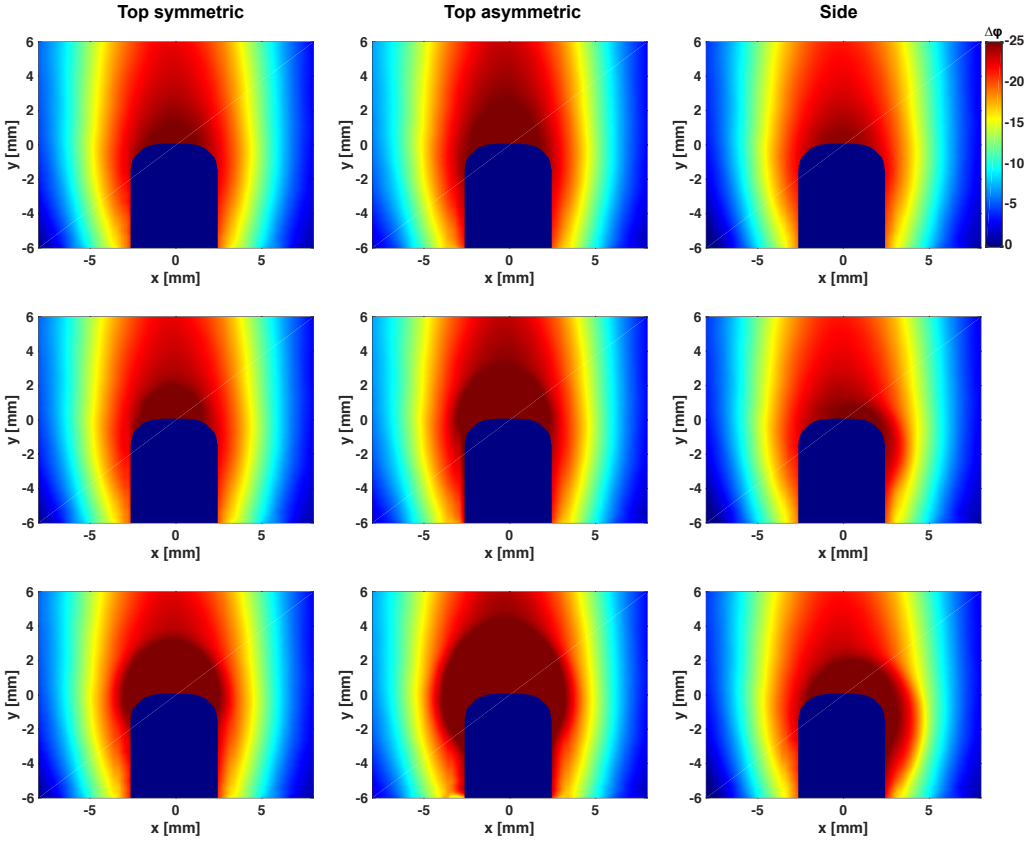

Figure 4: Optical phase difference fields illustrating the different ignition locations. Conditions: 20% H_2-air; T=295 K; P=101 kPa; heating rate=18 K/s.

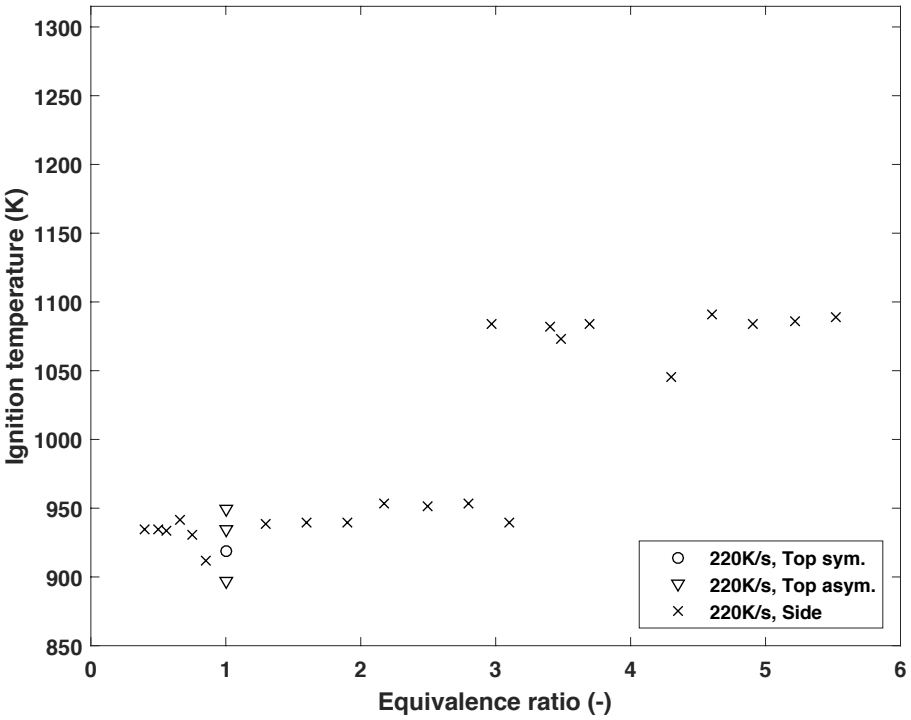

a) Ignition threshold with thermocouple

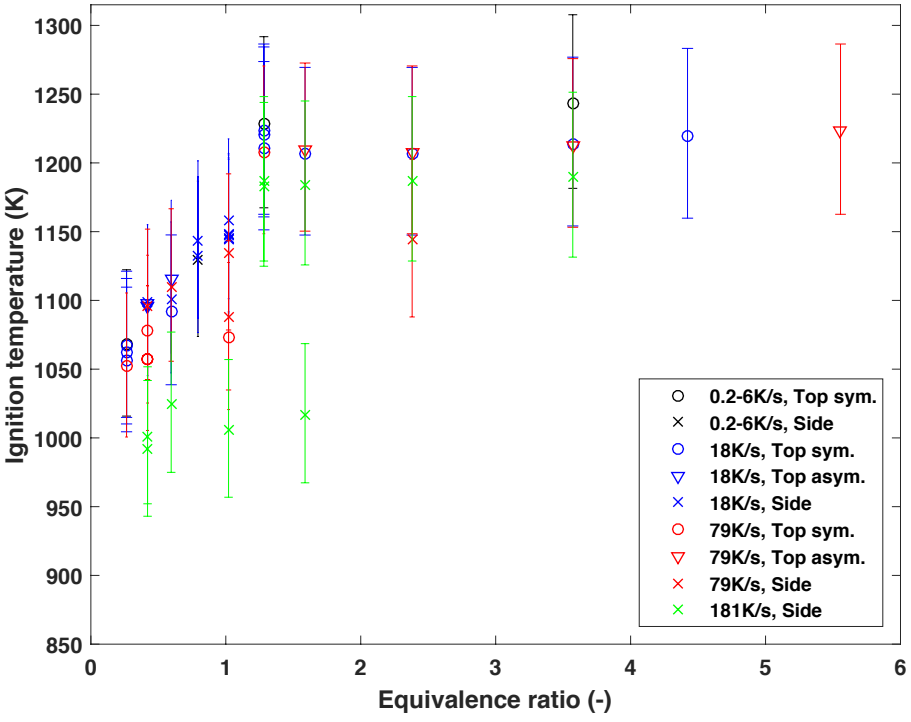

b) Ignition threshold with black body

Figure 5: Evolution of the ignition temperature threshold and ignition location as a function of equivalence ratio for hydrogen-air mixtures.

4.2 Numerical results

4.2.1 0-D simulations

The reaction models of Mével et al. (2009, 2011) and of Hong et al. (2011) were employed for the numerical simulations. Both mechanism were validated against extensive kinetics databases but demonstrate different behaviors in terms of the dependence of ignition delay-time on equivalence ratio. This aspect is illustrated in Figure 6 which shows the evolution of the delay time, defined as the time to OH* peak, as a function of temperature for mixtures with different hydrogen concentrations.

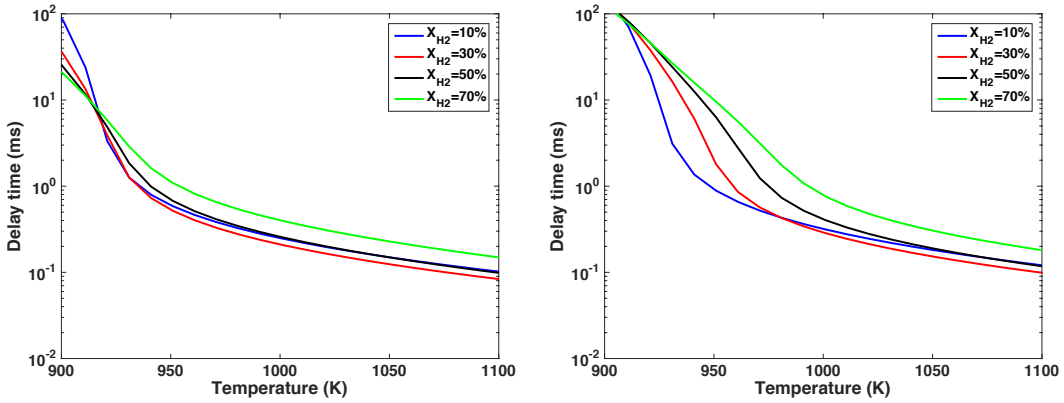

a) Mével et al. (2009) model b) Hong et al. (2011) model

Figure 6: Evolution of the constant pressure ignition delay-time of hydrogen-air mixtures as a function of temperature and hydrogen concentration.

4.2.2 2-D fields during ignition

A detailed analysis of the flow field during the ignition event was performed to identify important features in the flow such as thermal and hydrodynamic boundary layers, flow separation, thermal plume temperature, velocity distributions and chemical activity. Two-dimensional fields of temperature and velocity (magnitude), temperature contours and velocity vectors, and mass fractions of OH and H_2O_2 are shown in Figure 7 and Figure 8, respectively. Three different times, t=2.8995 s (shortly before ignition), t=2.899875 s (ignition kernel formation), and t=2.89995 s (early stages of flame propagation) display clearly the ignition evolution. The temperature contours are rescaled to cover the full range of temperature within the computational domain at each time.

Figure 7 a) shows the temperature and velocity (magnitude) fields obtained after 2.8995 s of heating, together with temperature isocontours at every 100 K from $100 \leq T \leq 938$K, and velocity vectors showing the buoyancy driven flow induced by the glow plug. In the vicinity of the hot surface there is a thermal boundary layer and above the glow plug, a thermal plume. In the separated region (above the glow plug) there is a thicker thermal boundary layer than on the side of the glow plug. The thermal plume outline is indicated by the outermost temperature contour (T=400 K). The velocity (magnitude) and velocity vectors illustrate the flow ocurring near and above the glow plug. Parcels of fresh cold

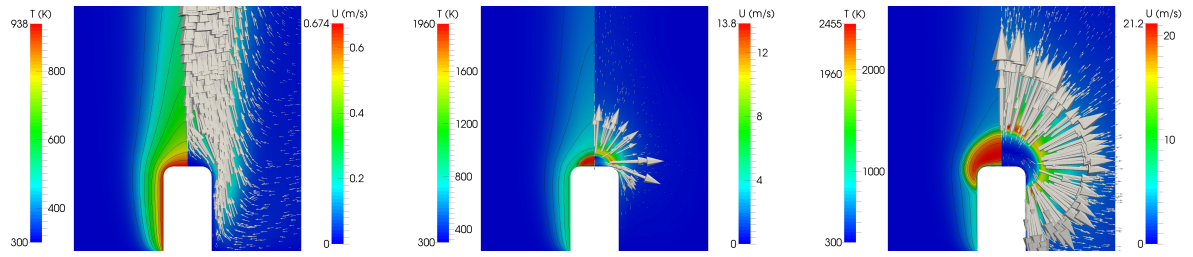

a) t=2.8995 s b) t=2.899875 s c) t=2.89995 s

Figure 7: Temperature and velocity (magnitude) field in the vicinity of the glow plug, temperature isocontours and velocity vectors for a stoichiometric hydrogen/air mixture at P=101 kPa, and T_o=300 K. a): t=2.8995 s (shortly before ignition). b): t=2.899875 s (ignition kernel formation). c): t=2.89995 s (early stages of flame propagation).

gas enter the thermal boundary layer from below and heat up slowly as they travel upward in close proximity to the glow plug surface. Once the parcels of gas reach the top of the glow plug, the flow separates, creating a region at the top of the glow plug where the gas is practically at rest. The gas outside this region continues to rise to the top of the combustion vessel, is forced to turn and creates a rather complex vortical flow field (not visible in Figure 7). Note that Figure 7 a) shows that chemical activity is confined to the top of the glow plug from very early on, where the temperature is highest, and convective losses are minimal. The temperature maximum in the domain ($T = 938$ K) corresponds to that of the glow plug surface. Further details of this flow field, and a thorough study of the ignition dynamics for *n*-hexane-air mixtures using simplified chemistry was performed by Melguizo-Gavilanes et al. (2016).

At t=2.8995 s, 375 μs later, an ignition kernel appears on the temperature field as closed

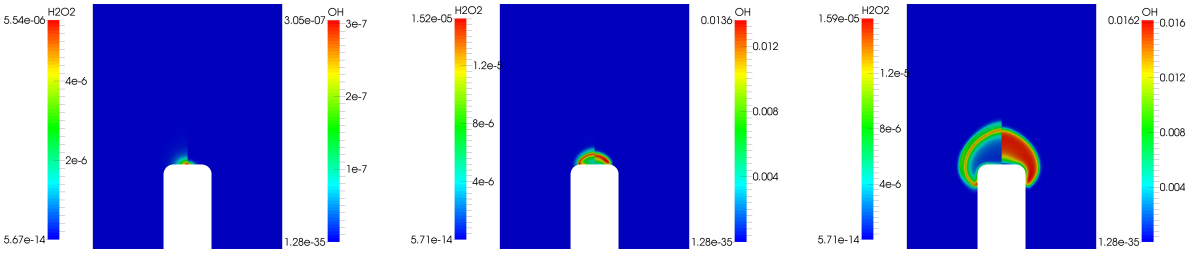

a) t=2.8995 s b) t=2.899875 s c) t=2.89995 s

Figure 8: Species mass fraction fields (H_2O_2 and OH) in the vicinity of the glow plug for a stoichiometric hydrogen/air mixture at P=101 kPa, and T_o = 300 K. a): t=2.8995 s (shortly before ignition). b): t=2.899875 s (ignition kernel formation). c): t=2.89995 s (early stages of flame propagation).

contours above the top of the glow plug. The energy release rate is strong enough to overcome diffusive and convective losses, and an internal maximum appears ultimately raising the temperature to 1960 K. A nascent flame can be observed in the temperature contours along with strong acceleration of the gas ahead of the ignition kernel evidenced by the velocity increase from 0.674 to 13.8 m/s over 375 μs (Figure 7 b). Additionally, the mass fractions of OH and H_2O_2 peak across the flame front ((Figure 8 b) as expected. The last frame (Figure 7 c), t=2.89995 s, shows the early stages of flame propagation.

Further acceleration of the gas from 13.8 to 21.2 m/s in an even shorter time interval, 75 μs, can be seen on the velocity fields. The maximum in velocity continues to be located immediately ahead of the flame, and the large volume expansion is evidenced by the size of the velocity vectors in the flow field. The shape of the flame is determined by the preferential propagation of the combustion front along the thermal plume where fresh combustible mixture is hottest (Boettcher et al. (2013)). The temperature contours show a nearly uniform high temperature region within the flame, except close to the glow plug surface where heat transfer occurs from combustion products towards the hot surface walls.

4.2.3 Ignition temperature threshold dependence on hydrogen concentration

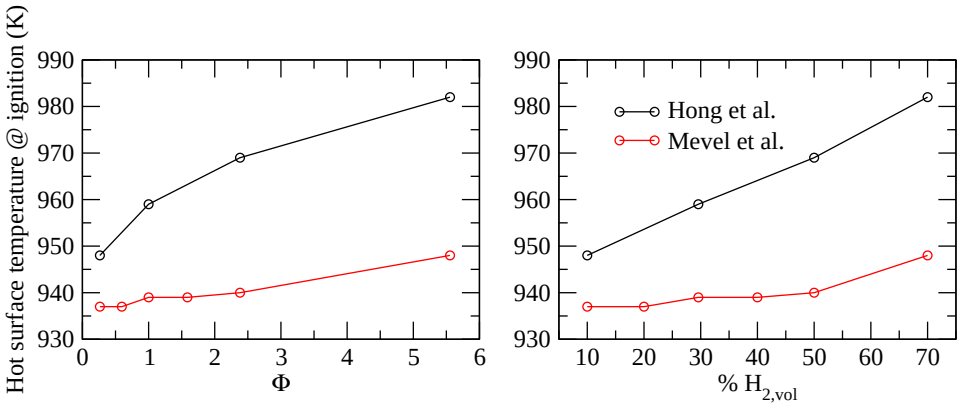

Figure 9: Effect of mixture concentration on ignition threshold for hydrogen-air mixtures from 2-D numerical simulations.

Figure 9 shows the effect of hydrogen concentration on the ignition threshold. The same qualitative trend as observed in the experiments was captured numerically. Results with both mechanisms show an upward trend with increasing equivalence ratio. However, the chemical model of Hong et al. exhibited a more pronounced dependence than Mével et al. with a surface temperature increase at ignition of 34 K and 11 K between the leaner and richest cases considered. This outcome was expected based on the 0-D results presented in Figure 9.

4.3 Discussion

Our experimental results place the surface temperature threshold for ignition of hydrogen-air mixtures at 1050 K at Φ=0.3 and at 1200 K at $\Phi \geq$1.3. According to Kumar (1989) study, the ignition threshold found was about 930 K and is independent of the hydrogen content between 10 and 50% of H_2 in air. Direct comparison of our experiments with Kumar's results is complicated by the difference between the two experimental configurations. Kumar employed a closed vessel and heated the mixtures with four slowly heated stainless steel rods. The fluid motion was very different that in the present experiments which could significantly influence the ignition temperature threshold. In addition, the

temperature was measured using thermocouples strapped to the hot surfaces which, according to our results, could significantly under-estimate the surface temperature. Issues with thermocouple temperature measurements include conduction losses along the leads, temperature gradients in the boundary layer, thermal contact resistance between hot surface and thermocouple, convective and radiative heat losses from the thermocouple and leads to the surroundings. Based on the present results, temperature on surfaces measured by contact thermocouples could be up to 150 K lower than the actual surface temperature. Experimental configurations closer to the present study include Roth et al. (2014) and Beyer and Markus (2012) who investigated the ignition of H_2-air mixtures by laser heated hot particles. In the case of 800 μm in diameter non-reactive Si_3N_4 spheres, Roth et al. (2014) reported an ignition threshold of about 1075 K and 1175 K for hydrogen-air mixtures containing respectively 5 and 60% of H_2 at ambient temperature and pressure. For reactive steel spheres of the same diameter, they observed an ignition threshold at higher temperatures, 1175 K for 5% H_2 and 1350 K for 60% H_2. For both materials, the increase of the threshold with hydrogen percentage was approximately linear. Beyer and Markus (2012) employed non-reactive iron oxide spheres of 500 to 1000 μm in diameter. The experiments were performed at 325 K and atmospheric pressure for mixtures containing between 5 and 30% of H_2 in air. For the smallest spheres, they reported an ignition threshold around 1300 K, and the largest spheres, the reported threshold dropped to about 1050 K. Due to the rather large uncertainty of the surface temperature measurements, the variation of the ignition threshold with hydrogen content cannot be inferred. Using a simplified 1-D model, Beyer and Markus (2012) studied the effect of the hot particle size and found an ignition threshold independent of the diameter for spheres larger than 5 mm and a strongly increasing threshold for diameters below 1 mm. The results of Roth et al. (2014) and Beyer and Markus (2012) are consistent with the present experimental observations. We speculate that because of the reactivity of the glow plug surface (316 stainless steel), the ignition threshold may be increased due to surface chemistry which enhances the recombination reaction of reactive radicals. The variation of temperature threshold with hydrogen content observed by Roth et al. (2014) is consistent with our experimental results. The numerical simulations also predict an increase in threshold with increasing hydrogen concentration but quantitative predictions will require considering surface chemistry as well as refining the gas phase model.

Concerning the ignition location, the numerical simulations indicate that the ignition event should preferentially occur at the top of the glow plug slightly above the surface. As explained in subsubsection 4.2.2, flow separation off the top edge of the glow plug, results in a small pocket of gas above of the top of the glow plug which remains essentially stagnant. This phenomenon creates conditions which are the most favorable for ignition to take place because the convection transport is minimum and losses are only due to diffusion except very close to the wall where the diffusion of the heat released by chemical reaction back to the wall prevents thermal runaway. In contrast to the simulations, where ignition was always observed to occur at the top, our experiments showed side ignitions. Such events were observed using high heating rates. Ignition on the side of the glow plug can be explained by assuming that the side of the glow plug surface has a much higher temperature than the top. At high heating rate, non-uniform heating of the glow plug

surface would likely be favored and ignition of the reactive mixture could take place as the gas travels upward along the side of the glow plug surface.

5. Conclusions

In the present study, the hot surface ignition of hydrogen-air mixtures was characterized in terms of ignition temperature threshold and ignition location on the surface of an electrically heated glow plug. Surface temperatures measured with a two-color pyrometer calibrated with a contact thermocouple and a black body light source demonstrated differences of up to 150 K which indicate that a thermocouple-based approach could result in a large under-estimation of the surface temperature at the ignition threshold. The effects of composition and hot surface heating rate were investigated experimental and numerically. A change of ignition threshold with equivalence ratio was observed with an ignition temperature of 1050 K at Φ=0.3 and of 1200 K at $\Phi \geq$1.3. The heating rate was found to influence the ignition location with high heating rate favoring ignition on the side of the glow plug. The present results indicate that hot surfaces with well defined properties are needed to enable a precise characterization of the ignition process in terms of temperature threshold and location on the hot surface. In order to make a direct comparison with the numerical simulations, a non-reactive surface should be used. Alternatively, the surface reactions should be accounted for in the simulations. In addition, a hot surface geometry that ensures a homogeneous heating should be employed. Spherical particles of small dimensions constitute a promising alternative to the commercial glow plug presently used. The study of hot surface ignition on materials relevant to industrial configurations demands to account for both surface chemistry and temperature non-homogeneity.

Acknowledgements

This work was performed at the Explosion Dynamics Laboratory at the California Institute of Technology and was supported by The Boeing Company through a Strategic Research and Development Relationship Agreement CT-BA-GTA-1. Josué Melguizo-Gavilanes was supported by the Natural Sciences and Engineering Research Council of Canada (NSERC) Postdoctoral Fellowship Program. The authors acknowledge the help of Andreas Kink, Technical University of Munich, for his help with the black body calibration.

References

Beyer, M. and Markus, D. (2012). Ignition of explosive atmospheres by small hot particles : Comparison of experiments and simulations. *Science and Technology of Energetic Materials*.

Boettcher, P. (2012). *Thermal Ignition*. PhD thesis, California Institute of Technology.

Boettcher, P., Menon, S., Ventura, B., Blanquart, G., and Shepherd, J. (2013). Cyclic flame propagation in premixed combustion. *Journal of Fluid Mechanics*, 735:176–202.

Boettcher, P. A., Mével, R., Thomas, V., and Shepherd, J. E. (2012). The effect of heating rates on low temperature hexane air combustion. *Fuel*, 96:392–403.

Bothe, H., Schenk, S., Hawksworth, S., Carleton, F., and Weinberg, F. (1999). The safe use of optics in potentially explosive atmospheres. In *Explosion Safety in Hazardous Areas, 1999. International Conference on (Conf. Publ. No. 469)*, pages 44–49.

Coates, P. (1981). Multi-wavelength pyrometry. *Metrologia*, 17(3):103.

Colwell, J. and Reza, A. (2005). Hot surface ignition of automotive and aviation fluids. *Fire Technology*, 41:105–123.

Council, C. R. (1983). *Handbook of Aviation Fuel Properties - CRC Report No. 530*. Society of Automotive Engineers, Warrendale, PA.

Demirdzic, I., Lilek, Z., and Péric, M. (1993). A collocated finite volume method for predicting flows at all speeds. *International Journal for Numerical Methods in Fluids*, 16:1029–1050.

Dubaniewicz, T. H. (2006). Threshold powers and delays for igniting propane and butane-air mixtures by cw laser-heated small particles. *Journal of Laser Applications*, 18(4):312–319.

Dubaniewicz, T. H., Cashdollar, K. L., and Green, G. M. (2003). Continuous wave laser ignition thresholds of coal dust clouds. *Journal of Laser Applications*, 15(3):184–191.

Dubaniewicz, T. H., Cashdollar, K. L., Green, G. M., and Chaiken, R. F. (2000). Ignition of methane-air mixtures by laser heated small particles. *Journal of Loss Prevention in the Process Industries*, 13(3-5):349–359.

Goodwin, D. G., Moffat, H. K., and Speth, R. L. (2015). Cantera: An object-oriented software toolkit for chemical kinetics, thermodynamics, and transport processes. http://www.cantera.org. Version 2.2.0.

Homan, H. S. (1981). Minimum mass of burning aluminum particles for ignition of methane/air and propane/air mixtures. *Proceedings of the Symposium (International) on Combustion*, 18:1709–1717.

Hong, Z., Davidson, D., and Hanson, R. (2011). An improved h2/o2 mechanism based on recent shock tube/laser absorption measurements. *Combustion and Flame*, 158:633–644.

Kemao, Q. (2004). Windowed fourier transform for fringe pattern analysis. *Appl. Opt.*, 43(13):2695–2702.

Kuchta, J. M., Bartkowiak, A., and Zabetakis, M. G. (1965). Hot Surface Ignition Temperatures of Hydrocarbon Fuel Vapor-Air Mixtures. *Journal of Chemical and Engineering Data*, 10(3):282–288.

Kumar, R. (1989). Ignition of hydrogen-oxygen-diluent mixtures adjacent to a hot, non-reactive surface. *Combustion and Flame*, 75:197–215.

Melguizo-Gavilanes, J., Boettcher, P., Gagliardi, A., Thomas, V., and Mével, R. (2015). Two-dimensional numerical simulation of the transition between slow reaction and ignition. *Proceedings of the 9th Joint US Sections Meeting of the Combustion Institute, 2015*.

Melguizo-Gavilanes, J., Nové-Josserand, A., Coronel, S., R., M., and Shepherd, J. (2016). Hot surface ignition of *n*-hexane mixtures using simplified kinetics. *Combustion Science and Technology*.

Menon, S., Boettcher, P., Ventura, B., and Blanquart, G. (2016). Hot surface ignition of c_6 and c_7 hydrocarbons in air. *Combustion and Flame*, 163:42–53.

Mével, R., Javoy, S., and Dupré, G. (2011). A chemical kinetic study of the oxidation of silane by nitrous oxide, nitric oxide and oxygen. *Proceedings of The Combustion Institute*, 33:485–492.

Mével, R., Javoy, S., Lafosse, F., Chaumeix, N., Dupré, G., and Paillard, C. E. (2009). Hydrogen-nitrous oxide delay time: shock tube experimental study and kinetic modelling. *Proceedings of The Combustion Institute*, 32:359–366.

Oran, E. and Boris, J. (2001). *Numerical Simulation of Reactive Flow*. Cambridge University Press.

Poinsot, T. and Veynante, D. (2005). *Theoretical and Numerical Combustion*. Edwards.

Rastogi, P. and Hack, E., editors (2015). *Phase Estimation in Optical Interferometry*. CRC Press.

Roth, D., Sharma, P., Haeber, T., Schiessl, R., Bockhorn, H., and Maas, U. (2014). Ignition by mechanical sparks: ignition of hydrogen/air mixtures by submillimeter-sized hot particles. *Combustion Science and Technology*, 186(10-11):1606–1617.

Saad, Y. (2003). *Iterative methods for sparse linear systems*. Society for Industrial and Applied Mathematics.

Smooke, M. D. (2013). The computation of laminar flames. *Proceedings of the Combustion Institute*, 34(1):65 – 98.

Touloukian, Y. and DeWitt, D. (1970). *Thermal radiative properties: metallic elements and alloys. IFI*. Plenum, New York.

Weller, H., Tabor, G., Jasak, H., and Fureby, C. (1998). A tensorial approach to continuum mechanics using object-oriented techniques,. *Journal of Computational Physics*, 12:620–631.